Journal of Magnetic Resonance 299 (2019) 49–58

Contents lists available at ScienceDirect

Journal of Magnetic Resonance

journal homepage: www.elsevier.com/locate/jmr

Phase contrast MRI of creeping flows using stimulated echo

Kulam Najmudeen Magdoom [a,*], Ahmad Zeinomar [b], Russell R. Lonser [c], Malisa Sarntinoranont [a,d], Thomas H. Mareci [b,d]

[a] Department of Mechanical and Aerospace Engineering, University of Florida, Gainesville, FL, USA
[b] Department of Biochemistry and Molecular Biology, University of Florida, Gainesville, FL, USA
[c] Department of Neurological Surgery, Wexner Medical Center, The Ohio State University, Columbus, OH, USA
[d] J. Crayton Pruitt Family Department of Biomedical Engineering, 1275 Center Drive, Biomedical Sciences Building, Gainesville, FL, USA

ARTICLE INFO

Article history:
Received 10 November 2018
Revised 10 December 2018
Accepted 13 December 2018
Available online 14 December 2018

Keywords:
Velocimetry
PC-MRI
Slow flows
Natural convection

ABSTRACT

Creeping flows govern many important physiological phenomena such as elevated interstitial fluid flows in tumors, glymphatic flows in the brain, among other applications. However, few methods exist to measure such slow flows non-invasively in optically opaque biological tissues *in vivo*. Phase-contrast MRI is a velocimetry technique routinely used in the clinic to measure fast flows in biological tissues, such as blood and cerebrospinal fluid (CSF), in the order of cm/s. Use of this technique to encode slower flows is hampered by diffusion weighting and phase error introduced by gradient hardware imperfections. In this study, a new PC-MRI technique is developed using stimulated echo preparation to overcome these challenges. Flows as slow as 1 μm/s are measured and validated using controlled water flow through a pipe at 4.7 T. The error in measured flow rate obtained by integrating the measured velocity over the cross-sectional area of the pipe is less than 10%. The developed method was also able to capture slow natural convection flows appearing in liquids placed inside a horizontal bore magnet. Monitoring the 4D velocity vector field revealed that the natural convection flows decay exponentially with time. This method could be applied in future to study creeping flows, e.g. in tissue.

1. Introduction

Creeping flows govern many important physiological phenomena. Elevated interstitial fluid flows, which govern drug distribution following direct infusion into the target biological tissue (i.e. convection enhanced delivery [1]), are in the order of tens of μm/s in the rat brain and mouse hindlimb tumors [2,3]. Naïve interstitial fluid flows in tumors, which play an important role in tumor metastasis, have been experimentally measured to range from 0.1 to 55 μm/s in rodents depending on the tumor type [4]. Glymphatic flows, which are thought to be responsible for waste clearance in the brain, are predicted to be around 100 μm/s [5] and flows in lymphatic vessels, which are one of the key determinants of tissue interstitial fluid pressure, has been measured to be around 50 μm/s in a mouse's ear [6], among other applications.

Most of the slow flow measurements in tissue reported in the literature were performed using limited depth of view optical techniques, such as fluorescence recovery after photobleaching (FRAP) or optical coherence tomography (OCT) techniques [6,7]. Slow flow measurements deep in the parenchyma have been reported using magnetic resonance imaging (MRI) by tracking MR visible contrast agents [8,9]. Such tracer tracking based techniques have several drawbacks: (1) they require introduction of a tracer which might be invasive and may change the natural flow in the system under study, and (2) velocity measurement is indirect, based on a model which separates flow related tracer displacement from that due to diffusion. This is particularly challenging for low Pèclet number flows where diffusion is on the same order as flow. Given the recent interest in understanding slow flows in the tissues, such as the brain glymphatics, a non-invasive direct 3D slow flow measurement technique is needed, which is capable of imaging deeper in the biological tissue *in vivo*.

To the best of our knowledge, MRI of spin displacement probability density function (also known as the propagator) and phase contrast MRI (PC-MRI) are the only two techniques currently available for direct flow measurement deep in tissues. Propagator imaging relies on the Fourier relationship between the complex MR signal attenuation with bipolar magnetic field gradients and the propagator [10]. The measured propagator is translated into velocity distribution by dividing it with the mixing time (i.e. time from the beginning of first flow-encoding gradient lobe to the next). This method has been applied so far to measure 1D flows as slow as

* Corresponding author at: Department of Mechanical and Aerospace Engineering, University of Florida, Gainesville, FL 32611, USA.
E-mail address: mkulam@ufl.edu (K.N. Magdoom).

https://doi.org/10.1016/j.jmr.2018.12.009
1090-7807/

200 nm/s of slowly diffusing tracer particles placed in a cylindrical Couette cell [11], flows approximately 20 μm/s in tissue mimicking packed bed phantoms [12] and 0.67 mm/s in plant tissue [13]. However, the method maybe time consuming, especially for imaging creeping flows since the MR signal needs to be sampled repeatedly with varying gradient strengths oriented in 3D to fully resolve the small displacements resulting from slow flows in 3D. Given the effects of flow appear in the phase of the complex MR signal attenuation due to the Fourier shift theorem, it is difficult to isolate the flow related phase shift from that due to gradient hardware imperfections whose effects scale with the applied gradient strength. These challenges may limit its use *in vivo*.

PC-MRI is an MR velocimetry technique regularly used in the clinic to measure flows in tissues, such as the blood and cerebrospinal fluid (CSF) [14–17]. It does not involve exogenous tracers and allows for direct velocity measurements in an opaque material such as the tissue. It is similar to the propagator imaging with bipolar magnetic field gradients used to induce linear velocity dependent phase in gradient echo MR images which is isolated from other phase contributions to obtain the mean velocity in a voxel instead of the velocity distribution. In the PC-MRI technique, the flow-encoding gradient strength is held constant and oriented in a tetrahedron to encode flows in 3D, thereby making it faster than the propagator method.

Despite its clinical applicability, encoding slower flows with PC-MRI is challenging since it requires application of very large gradient strength and/or duration. This increases the diffusion weighting in the scan resulting in decreased velocity sensitivity. It also exacerbates the effect of gradient hardware imperfections due to eddy currents induced in surrounding conductors [18], mechanical resonance of gradient coil [19], and gradient concomitant fields [20] resulting in non-zero position dependent velocity irrespective of flow, and velocity errors in flowing regions. Position dependent phase errors are usually corrected by measuring them locally in a static region of interest and subtracting them globally on the entire imaging slice following error interpolation [20,21]. However, velocity errors in flowing regions remain uncorrected and might be on the same order as slow flow velocities of interest.

A PC-MRI sequence minimizing both diffusion weighting and gradient hardware errors, while maximizing flow weighting, would be useful for measuring very slow flows *in vivo*. Velocities measured in typical clinical PC-MRI scans range from 30 to 200 cm/s [17], which is appropriate for fast CSF and blood flows. Huang et al. used spin echo phase contrast MRI for improved flow sensitivity to measure slow fluid flows on the order of a few mm/s imposed in a porous foam. Gradient hardware induced phase errors in the velocity map were removed using a separate acquisition without flow which may not be feasible for *in vivo* applications [22]. Recently, Samuel and co-workers reported interstitial/blood flow measurements as low as 20 μm/s in murine hind limb tumor using gradient echo PC-MRI albeit with low precision due to large diffusion weighting in the scans [23]. To the best of our knowledge, this is currently the slowest velocity reported to have been measured using PC-MRI.

In this study, a PC-MRI technique with stimulated echo (STE) preparation, capable of measuring flows as slow as 1 μm/s, is developed by minimizing the scan diffusion weighting and phase errors introduced by gradient hardware imperfections. The method is tested using a controlled pipe flow experiment and applied to study natural convection flows appearing in liquids placed inside a horizontal bore magnet. Future applications include investigating flows in tissues, such as glymphatic flows in the brain, elevated interstitial fluid flows in tumors, convection enhanced delivery flows, and pulsatile motion of brain parenchyma during cardiac and respiratory cycles [24].

2. Materials and methods

2.1. Flow imaging theory

Phase induced on spins steadily flowing with velocity, $\vec{v}$, by a bipolar gradient, $\vec{G}_{flow}(t)$, consisting of two unipolar gradients, $\vec{g}(t)$, of duration, δ, separated by time, Δ, is given by [25] (see Appendix A),

$$\phi = -\gamma \vec{v} \cdot \int_0^{\Delta+\delta} t\,\vec{G}_{flow}(t)dt = \vec{v} \cdot \vec{q}\,\Delta, \qquad \vec{q} = \gamma \int_0^{\delta} \vec{g}(t)dt \tag{1}$$

Velocity is measured using the above relation by isolating the flow dependent phase from other contributions such as from sample susceptibility, radiofrequency (RF) pulse, etc.

Measuring 3D velocity requires four acquisitions per voxel with flow-encoding gradient polarities along the imaging gradient axes (i.e. read, phase and slice) systematically varied according to the Hadamard encoding given in Table 1, which provides greater velocity sensitivity with fewer acquisitions than simple four or six-point velocity encoding [25]. Flow weighting is characterized by the user-controlled velocity encoding anti-aliasing factor, v_{enc}, which for a given flow-encoding gradient is the velocity at which the phase begins to wrap to ±π. For Hadamard encoding this is given by [26],

$$v_{enc} = \frac{\pi}{4\left|\vec{q}\right|\Delta} \tag{2}$$

The individual velocity components along read, phase and slice gradient axis are obtained by complex division of the four velocity encoded images as shown below,

$$\frac{v_{read}}{v_{enc}} = \frac{\arg\left(\frac{S_1 \cdot S_4}{S_2 \cdot S_3}\right)}{\pi} \quad \frac{v_{phase}}{v_{enc}} = \frac{\arg\left(\frac{S_1 \cdot S_3}{S_2 \cdot S_4}\right)}{\pi} \quad \frac{v_{slice}}{v_{enc}} = \frac{\arg\left(\frac{S_1 \cdot S_2}{S_3 \cdot S_4}\right)}{\pi} \tag{3}$$

where S_i is the complex MR image from the ith acquisition in the Hadamard encoding table shown in Table 1 and arg is the complex argument (i.e. phase angle of the complex number).

The smallest measurable velocity by this technique is limited by the amount of phase noise present in the flow weighted scan. Velocity dependent phase should exceed the phase noise standard deviation present in the scan which is equal to the inverse of the signal-to-noise ratio (SNR) of magnitude images [25] resulting in the following relation,

$$\frac{\pi v}{v_{enc}} > \frac{1}{SNR} \tag{4}$$

$$\Rightarrow v > \frac{1}{\pi}\left(\frac{v_{enc}}{SNR}\right) \tag{5}$$

Thus, measuring slow flows requires smaller v_{enc} and/or higher SNR. A major source of signal loss in pulsed field gradient experiments is from phase dispersion due to spin diffusion during the mixing period, Δ. Diffusion weighting in the scan is given by the b-value [10],

Table 1
Hadamard encoding table for flow imaging showing the polarity of effective flow-encoding gradient on each of imaging gradient axes (read, phase and slice) for the four acquisitions [25].

Acquisition #	Read	Phase	Slice
1	+	+	+
2	−	−	+
3	−	+	−
4	+	−	−

$$b = \left|\vec{q}\right|^2 \Delta \quad \text{for} \quad \Delta \gg \delta \tag{6}$$

The quadratic dependence of b-value on $\left|\vec{q}\right|$ emphasizes the advantage of minimizing $\left|\vec{q}\right|$ over Δ for reducing diffusion weighting. The use of longer Δ increases the sensitivity to flow related spin displacement, which scales by Δ, but decreases the sensitivity to diffusion, which scales by $\sqrt{\Delta}$. The long mixing period afforded by the stimulated echo due to long T_1-relaxation time of samples such as the tissue allows minimizing $\left|\vec{q}\right|$ while increasing Δ to compensate for the lost velocity sensitivity.

Eddy currents generated in the magnet bore and mechanical resonance of gradient coils cause errors in flow-encoding gradient time integrals, which result in a linear phase error (ϕ_e) across the imaging field of view which could be misinterpreted as true velocity [18]. The resulting error in measured velocity, v_e, is given by,

$$v_e = v_{enc}\left(\frac{\phi_e}{\pi}\right) \tag{7}$$

2.2. Pulse sequence design

The stimulated echo phase contrast MRI pulse sequence with flow compensated imaging gradients is shown in Fig. 1. Coherence image artifacts due to free induction decay (FID) from the third RF pulse were eliminated using slice crusher gradients and/or 2-step phase cycling of the second and third RF pulses ($\varphi = \pm y$ with the receiver phase kept at $+x$). Phase cycling helps reduce diffusion weighting caused by the crusher gradients and hence increases the velocity sensitivity. Phase encode and read dephase gradients were placed before the flow-encoding gradient to minimize image misalignment across the flow acquisitions due to varying eddy currents generated with flow-encoding gradient polarity switching.

Flow compensation was performed for imaging gradients to improve SNR by rephasing flow dependent phase dispersion induced by these gradients. The phase-encode and read dephase gradients were split into two gradient lobes of opposite polarity with identical duration, T, as shown in Fig. 1. The amplitudes of the split gradient lobes were adjusted such that their zeroth moment satisfied the Nyquist criterion to encode space while their first moment, including the readout gradient, became zero at the echo time for flow compensation resulting in the following,

$$G_+^{pe} = M_0\left(\frac{3\mathrm{T} + 2t_e}{2\ \mathrm{T}^2}\right),\ G_-^{pe} = M_0\left(\frac{\mathrm{T} + 2t_e}{2\ \mathrm{T}^2}\right) \tag{8}$$

$$G_+^{rd} = G_{ro}\left(\frac{t_e}{\mathrm{T}}\right),\ G_-^{rd} = G_{ro}\left(\frac{t_e + \mathrm{T}}{\mathrm{T}}\right) \tag{9}$$

where $G_{+/-}^{pe}, G_{+/-}^{rd}$ are the amplitudes for the positive/negative phase encoding and read dephase gradient lobes respectively, M_0 is the zeroth moment of the phase encode gradient to be satisfied, t_e is the time between the end of the second gradient lobe and echo, and G_{ro} is the amplitude of the readout gradient to be satisfied.

The effect of magnetic fields persisting after the end of the flow-encoding gradient pulse, due to eddy currents and mechanical resonance, was reduced by using the following time symmetry in the pulse sequence. Position dependent phase accumulated by the spins due to persisting magnetic fields, generated from the flow-encoding gradient pulse in the first TE/2 interval, was refocused at the echo time in the second TE/2 interval by equalizing the time interval, τ, between the second flow-encoding gradient pulse and readout/slice select gradient. The phase cancellation requires that the persisting field from each flow-encoding gradient decay before the next flow-encoding gradient pulse is applied (i.e. Δ is much longer than the time constants associated with the decaying fields), and the gradient echo formed under the STE for imaging is unaffected by the flow-encoding gradient. The use of STE allowed long Δ, sufficient for the persisting fields generated by the first flow-encoding gradient to decay. Gradient echo shifting from persisting fields with short time constants was alleviated by adjusting τ between the flow and readout/slice select gradients, while the effect of longer time constants was removed through post-processing by estimating the linear phase error in a static phantom and applying it on the whole image. Given these errors scale with v_{enc} (Eq. (7)), they are very small compared to traditional PC-MRI techniques which typically have v_{enc} several orders of magnitude higher than the present method [17].

2.3. Flow phantoms

2.3.1. Pipe flow

A syringe pump (Model 33, Harvard Apparatus, Holliston, MA) with a 10 mL syringe (BD, Franklin Lakes, NJ) attached to a silicone rubber tubing (ID = 6.35 mm, OD = 12.7 mm, length = 25 ft, McMaster-Carr, Douglasville, GA) was used to pump deionized (DI) water at a constant flow rate of 2 and 10 μL/min during MR imaging. The infusion pump was calibrated outside the magnet by weighing the infusate delivered at the set flow rate of 10 μL/min which resulted in errors less than 15%.

Both the ends of the tubing were sealed using quick connect plugs (Product # 5012K44, McMaster-Carr, Douglasville, GA) and

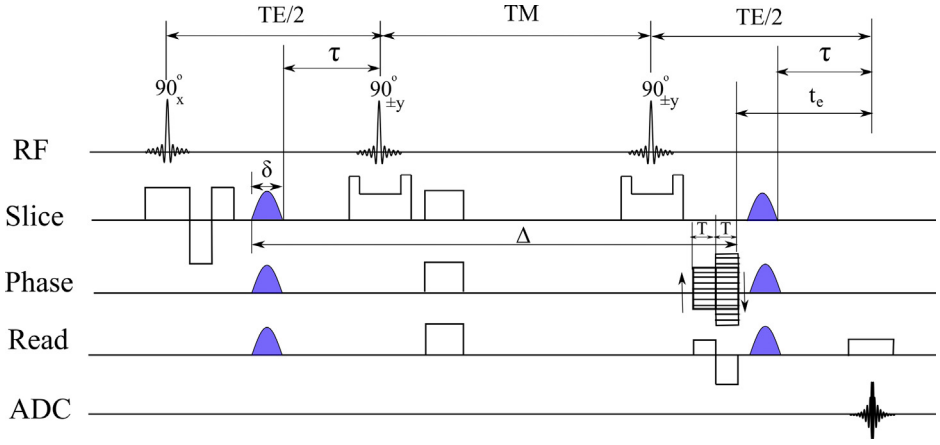

Fig. 1. Flow compensated stimulated echo phase contrast MRI pulse sequence with flow encoding gradient shaded in blue. TE – echo time, TM – mixing time and τ – gradient balancing time. (For interpretation of the references to color in this figure legend, the reader is referred to the web version of this article.)

heat shrink tubing, and opened for flow using quick connect sockets (Product # 5012K44, McMaster-Carr, Douglasville, GA). Evansblue dye (MP Biomedicals, LLC, Solon, OH) was added to the DI water to monitor bubbles in the line. Water filled silicone tubing was passed through two holes in a custom 3D printed solid cylinder (see Fig. 2, Part (A)) to drain into a beaker placed outside the magnet. Two additional holes were printed in the solid cylinder to hold two 5 mm NMR tubes (Wilmad-LabGlass, Vineland, NJ) filled with 0.6% hydrogel (Trevigel 500, Trevigen. Inc, Gaithersburg, MD) to suppress bulk water motion and monitor and correct position dependent background phase errors if any. Those holes were placed at the edges of the phantom where the linear phase errors are the largest for maximum sensitivity. Apart from damping bulk water motion, 0.6% hydrogel was chosen since its T_1 relaxation time at 4.7 T (~2175 ms) and diffusivity ($\sim 1.9 \times 10^{-3}$ mm^2/s) is similar to that of water [27]. This resulted in uniform flow sensitivity across the field of view which is dependent on the sample T_1 relaxation time and diffusivity assuming $TE \ll T_2$. Assuming the spins fully recovered before each shot (i.e. $TR \gg TM + T_1$), lower MR signal from a sample with a shorter T_1 and larger diffusivity results in a reduced flow sensitivity and vice versa.

The imposed velocity, v, along the long axis of the silicone tubes oriented at a polar angle, θ, and azimuthal angle, Φ, with respect to the imaging gradient axes was decomposed into the following Cartesian components measured in the flow scan,

$$v_x = v \sin\theta \cos\Phi \quad v_y = v \sin\theta \sin\Phi \quad v_z = v \cos\theta \tag{10}$$

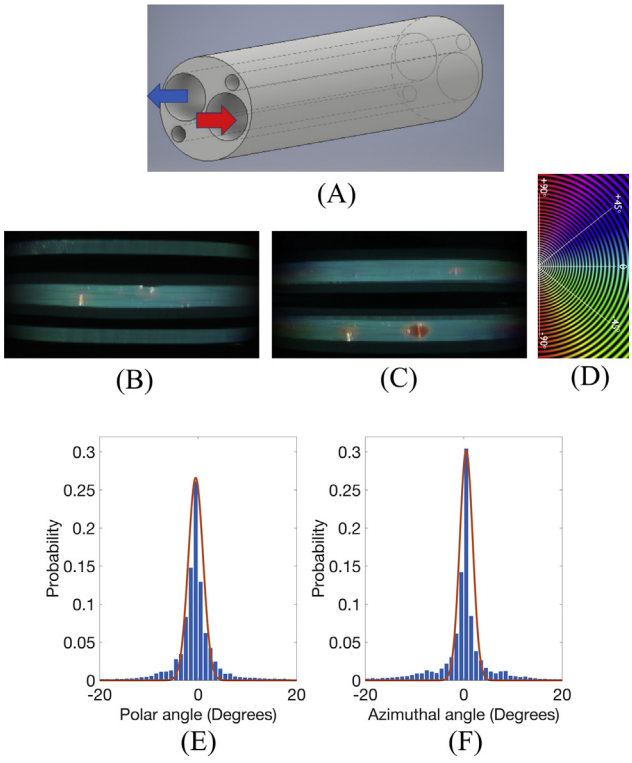

Fig. 2. Experimental setup of pipe flow measurement along with orientation information. (A) 3D rendering of the flow phantom used to hold the silicone tubing marked by blue and red arrows signifying the flow direction, and hydrogel tube marked by the smaller holes adjacent to it, (B) Polar and (C) azimuthal orientation map calculated using the OrientationJ plugin [32] in Fiji software [33] based on sagittal and coronal MIPs of 3D FLASH images of sample respectively, (D) Color map used to display orientation, Probability histogram of (E) polar and (F) azimuthal angles overlaid with the normal distribution fit ($[\mu_\theta, \sigma_\theta] = [-0.5°, 1.5°]$, $[\mu_\phi, \sigma_\phi] = [0.5°, 1.32°]$). (For interpretation of the references to color in this figure legend, the reader is referred to the web version of this article.)

Peak velocity, v_p, in a tube of cross-sectional area, A, with an imposed volumetric flow rate, Q, is given by [28],

$$v_p = \frac{2Q}{A} \tag{11}$$

The dimensionless Reynolds number, *Re*, which helps predict the nature of pipe flow (laminar for $Re < 2000$ else transition into turbulence [28]) is given by,

$$Re = \frac{v_p d}{v} \tag{12}$$

where d is the diameter of the tube and v is the kinematic viscosity of the fluid. Entrance length for laminar pipe flow, which is the distance at which flow becomes fully developed,

(i.e. parabolic velocity profile) is given by [28],

$$L_e = \frac{Red}{30} \tag{13}$$

2.3.2. Natural convection

Natural convection induced by temperature gradients present in the horizontal magnet bore was studied by imaging two 15 mL cylindrical falcon tubes (BD, Franklin Lakes, NJ) filled with either deionized water or 0.6% hydrogel, which served as a static phantom. Tubes were inserted into two holes printed in custom 3D printed solid cylinder which was placed inside the radiofrequency (RF) coil. The dimensionless Rayleigh number, Ra, which characterizes such buoyancy driven flows is given by the following relation [29],

$$Ra = \frac{g\alpha\Delta T R^3}{v\kappa} \tag{14}$$

where g is acceleration due to gravity, α, v, κ are the thermal expansion coefficient, kinematic viscosity and thermal diffusivity of the fluid, R is the radius of the tube and ΔT is the temperature difference between the fluid and its surroundings.

2.4. MR measurements

All MRI measures were collected on a 330 mm ID 4.7 T horizontal bore magnet (Oxford Instruments, Abingdon, UK) with an RRI BFG-200/115-S14 gradient set (Resonance Research, Billerica, MA) connected to an Agilent VNMRS imaging console controlled by VnmrJ3.1A software (Agilent Technologies, Santa Clara, CA). RF was transmitted and received using 38 mm inner diameter quadrature birdcage coil (Varian, Inc, Palo Alto, CA).

2.4.1. Pipe flow

The sample T_1 was measured prior to flow imaging to determine the appropriate mixing time, Δ, for flow encoding. T_1 measurement was made using inversion recovery spectroscopy pulse sequence with the following inversion times, TI = 312.5, 625, 1250, 2500, 5000, 10,000 ms. Orientation of the silicone tubes with respect to the Cartesian imaging axes of the flow scan was determined a priori using a 375 μm isotropic sagittal 3D gradient echo imaging (i.e. fast low angle shot, FLASH) of the sample acquired with TR/TE = 50/1.7 ms, flip angle = 45° and field of view (FOV) = 72 mm × 36 mm × 36 mm.

Flow imaging data was acquired for two 8 mm thick axial slices in the center straight section of the tubes with FOV = 32 mm × 32 mm, matrix size = 96 × 96, TR/TE = 4500/28 ms, NEX = 2, half-sine shaped flow encoding gradient with δ = 0.5 ms of strength = 120 mT/m to minimize eddy currents (i.e. by slow sinusoidal ramping the gradients) and Δ = 2000 ms resulting in a $v_{enc} \approx 38$ μm/s. Delay time, τ, between flow and imaging gradients was set to 2 ms in order for the short eddy current time constants to decay before

readout. The sequence was repeated for two different flow rates (Q = 2 and 10 μL/min). Prior to starting the pump, the sample was allowed to sit inside the magnet bore for approximately 5.5 h in order for the natural convection flows to settle down.

2.4.2. Natural convection

Flow imaging data for the natural convection sample was acquired for a single 8 mm thick axial slice with a FOV = 32 mm × 16 mm, matrix size = 128 × 64, NEX = 2, TR/TE = 3000/28 ms, a half-sine shaped flow encoding gradient with $\delta = 0.5$ ms of strength = 120 mT/m, and $\tau = 2$ ms. Decay of natural convection as the sample was reaching thermal equilibrium with the magnet bore was studied by repeating the flow imaging sequence every 30 min over a period of three hours. Mixing time, Δ, for the first 1.5 h was set to 500 ms ($v_{enc} \approx 150$ μm/s) to reduce phase aliasing from faster flows in the beginning and increased to 1500 ms for the next 1.5 h to achieve greater sensitivity ($v_{enc} \approx 50$ μm/s) for slower flows present at later times.

2.5. Data processing

Velocities were computed by dividing the complex MR image according to Eq. (3) using an in-house software written in IDL programming language (Harris Geospatial Solutions, Broomfield, Colorado). Phase unwrapping was performed on the individual components of velocity if necessary using the algorithm outlined in [30]. Phase error due to gradient echo shifting during readout or shorter mixing times was removed through post-processing by fitting the error to a linear function using the least squares routine, *curvefit*, in IDL. The error was measured in a region of interest (ROI) encompassing the static phantom and subtracted from the measured velocity map. The obtained velocity was visualized in 3D using vector plots generated with open source *Paraview* software [31].

In the pipe flow experiment, the orientation of tubes in the pipe flow experiment with respect to the imaging reference frame were calculated to compare the measured velocities with the values predicted based on the imposed flow rate and pipe cross-sectional area using Eqs. (10) and (11). The analysis was performed by applying the *OrientationJ* plugin [32] in Fiji software [33] on the sagittal and coronal maximum intensity projections (MIPs) of 3D FLASH images of sample to calculate the polar and azimuthal orientation of the tubes respectively.

Accuracy of the flow measurement was evaluated by comparing the volumetric flow rate, Q, for pipe flow along the long axis (i.e. a) of the tube with the value set in the pump where Q is defined by the following relation,

$$Q = \int\int v_a \, dx \, dy \tag{15}$$

3. Results

The average T1 relaxation time of the pipe-flow sample measured using an inversion recovery pulse sequence is approximately 2800 ms. Results of the tube orientation analysis for the pipe flow phantom are shown in Fig. 2. Orientation maps of both sagittal (Fig. 2B) and coronal (Fig. 2C) 2D MIP images show the long axis of the tube is parallel to the imaging axes. The colormap for orientation angle is shown in Fig. 2D where each ray in the semicircle is colored based on the angle it subtends with the horizontal. Apparent bending of the tube at the edges of the imaging field of view could be due to gradient non-linearity which is specified to vary by ±20% within a 80 mm diameter spherical volume for the gradient coil used in this study. Changing orientation in a few voxels in

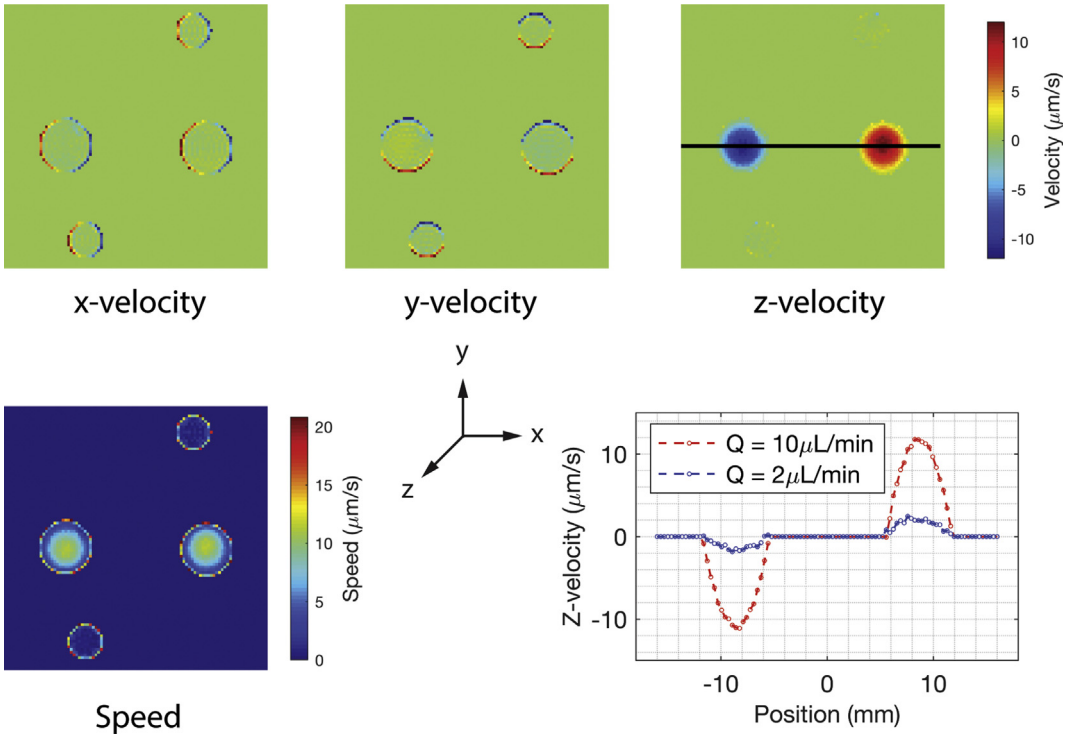

Fig. 3. PC-MRI measurement of water flow through pipes using stimulated echo. Two large tubes in the images contain water, and smaller tubes contain 0.6% hydrogel to serve as static control. (Top row) X, Y, Z components and (Bottom left) magnitude of velocity obtained with the imposed flow rate equal to 10 μL/min ($Re \approx 0.05$) along the long axis of the tube. (Bottom right) Plots of Z-velocity obtained at two different flow rates (2 and 10 μL/min) along the black midline shown in the Z-velocity map.

the middle of the tube is due to signal pileup artifacts resulting from magnetic susceptibility changes caused by bubbles present within the sample. Histogram analysis of the MIP images shows that the mean polar (Fig. 2E) and azimuthal (Fig. 2F) angle are -0.5° and $+0.5^\circ$ with a standard deviation of $1.5^\circ$and -1.32°, respectively. From Eq. (10), flow is expected to be one-dimensional along the long axis of the silicone tube (i.e. z-axis) since the maximum transverse velocity component (i.e. v_x, v_y) for the faster 10 μL/min is expected to be less than 0.1 μm/s, which is below the sensitivity of the flow imaging scan.

Background phase offset is observed in the static phantom in the read velocity component (i.e. v_x) with a slope and intercept approximately equal to −0.01 rad/mm and 0.2 rad respectively, with goodness of fit measure, r^2, approximately equal to 0.7. This translates to offsets in velocity equal to 2.45 ± 2 μm/s across a 32 mm FOV which is subtracted from the measured velocity. Reynolds number for the flow is approximately 0.01, 0.05 and entrance length is 2, 10 μm for Q = 2, 10 μL/min respectively, effectively rendering the flow laminar and fully developed in the imaging field of view for both the flow rates. The three velocity components obtained with an imposed flow rate of 10 μL/min for one imaging slice is shown in Fig. 3. Measured flow is one dimensional as expected along the long axis of the tube (i.e. z-velocity), and in equal and opposite directions corresponding to incoming and outgoing water flow. The error in the velocity, given by the z-velocity standard deviation measured over a ROI drawn in the static hydrogel, is approximately equal to 0.2 μm/s. Line plots of z-velocity along the mid-line intersecting the tubes in Fig. 3 shows parabolic velocity profiles with peak velocities matching with the predicted values for both imposed flow rates. 3D velocity vectors for both the slices for flow at Q = 10 μL/min, shown in Fig. 4, exhibit a paraboloid velocity profile. Three-dimensional animation of flow vector field is provided in the Supplementary movie S1. Volumetric flow rates, calculated by integrating the z-velocity over a ROI encompassing the entire cross-sectional area of the water filled tube, along with the values set in the pump are reported in Table 2. Errors in measured flow rate from the set value are less than 10%.

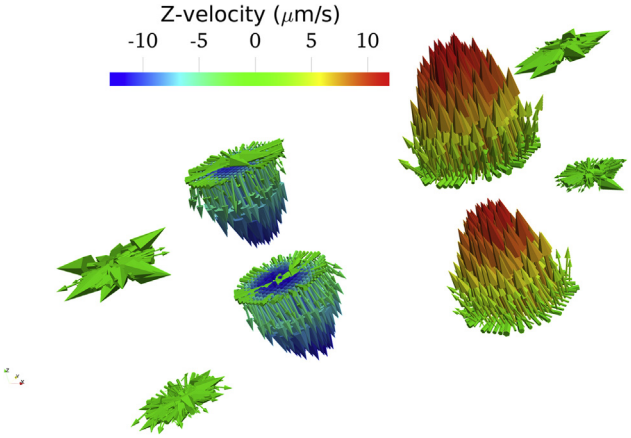

Fig. 4. 3D vector plots of water flow through the pipe at 10 μL/min ($Re \approx 0.05$) along with 0.6% hydrogel. Vectors are colored based on the Z-component of the velocity. Green arrows at the edges are due to the spurious velocities observed at the boundary. (For interpretation of the references to color in this figure legend, the reader is referred to the web version of this article.)

Table 2
Comparing the MR measured flow rate along the long axis of the tube over a region of interest encompassing the silicone tube with the flow rate set on the pump for pipe flow experiments.

Experiment #	Set flow rate (μL/min)	Measured inflow rate (μL/min)	Measured outflow rate (μL/min)
1	10	+10.99	−10.91
2	2	+1.94	−2.01

Background phase error in the natural convection phantom is not apparent in its measured velocity map likely due to reduced sensitivity since the static phantom did not span the entire FOV. Rayleigh number for natural convection at the beginning of the experiment was approximately 6000 given the sample tempera-

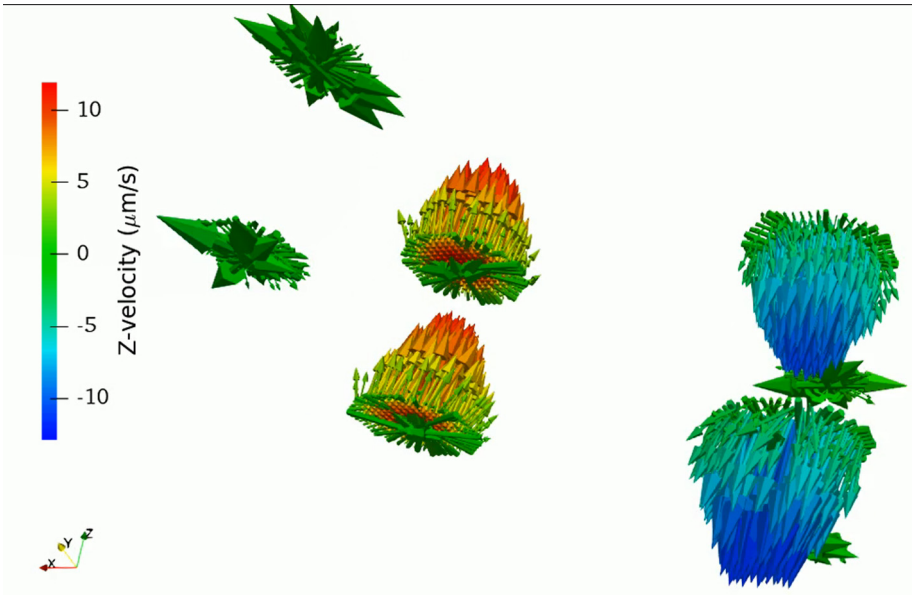

Supplementary movie S1. 3D animation of the flow vector field of water flow through the pipe at 10 μL/min ($Re \approx 0.05$) along with 0.6% hydrogel. Vectors are colored based on the Z-component of the velocity. Green arrows at the edges are due to the spurious velocities observed at the boundary.

ture was 23 °C before it was placed in the magnet bore at 17 °C, both of which were measured using a thermometer. Velocity components obtained for natural convection in a water filled cylinder beside a 0.6% hydrogel, approximately 45 min after placement in the magnet bore, are shown in Fig. 5. Measured velocities show a primary circulation along the long axis of the cylinder (i.e. z-axis) with weaker secondary flows in the x – y plane. Plots of axial velocity along the vertical mid-line in Fig. 5 show an S-shaped velocity profile whose peak has reduced with time. 3D velocity vectors for the measured flow are shown in Fig. 6 at approximately 45 min after the sample placement in the magnet. Three-dimensional animation of flow vector field is provided in the Supplementary movie S2. The vector plot shows a 3D asymmetric vortex close to the wall of the tube. Consecutive flow measurements show that the velocity pattern is maintained but decayed in magnitude as time progresses. A plot of the velocity magnitude over time, averaged over an ROI in the water filled tube, (Fig. 5) shows that the speed decays exponentially with a time constant approximately equal to 2 h.

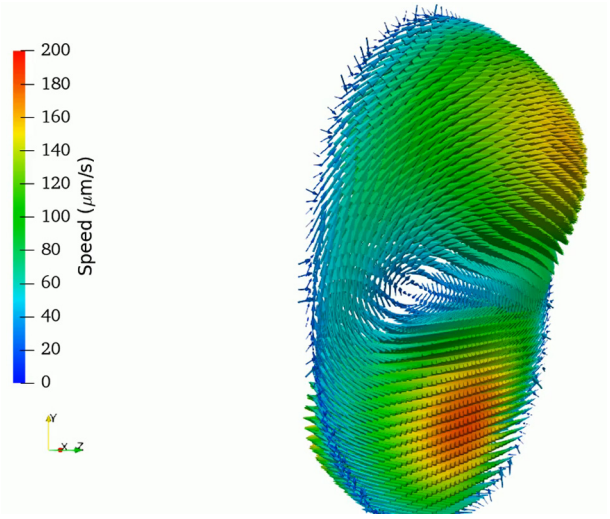

Supplementary movie S2. 3D animation of natural convection inside a horizontal cylindrical tube filled with water at approximately 45 min after the sample was placed in the magnet bore. Vectors are colored based on the velocity magnitude.

Spurious velocities averaging approximately 10 μm/s in magnitude are detected along the edges of static and flowing tubes in both pipe flow and natural convection experiments. Velocity is normal to the wall and inward, appearing to contract the tube. Since the velocity normal to an impermeable static wall should be zero [28], this displacement is likely unrelated to flow. Given the effective velocity, v_{eff}, measured includes contribution from sample acceleration, a, (i.e. $v_{eff} \approx v + a\Delta$ for $\Delta \gg \delta$), the observed boundary effect might have resulted from acceleration of the tube wall from sample vibration with gradient switching.

4. Discussion

A new PC-MRI method with stimulated echo preparation was developed to measure creeping flows non-invasively in optically opaque media such as a biological tissue. Effect of diffusion weighting which randomizes the phase was minimized using a stimulated echo preparation while the phase errors arising from gradient imperfections was reduced by placing a time symmetry in the pulse sequence. The method was capable of measuring flows as slow as 1 μm/s with potential *in vivo* applications in the brain and other organs.

4.1. Pipe flow

Results from pipe flow measurement agreed with known physical principles. The axial velocity profile was parabolic as expected with errors in flow rate less than 10%. Sources of this error include noise in the flow measurement, fluctuations in pump output, and inaccuracies in the measured syringe diameter used by the pump to set the target flow rate. The MR measured flow rate was compared with the set flow rate which might be different from the actual despite the calibration performed outside the magnet. Direct measurement of output flow rate during imaging for example by weighing the delivered infusate is challenging for very slow flow rates because fluid may evaporate before sufficient mass can be obtained above the sensitivity of the scale. Alternative techniques such as using a rotameter attached at the output could be employed in future for accurate flow rate measurement. The effect of tube curvature outside the imaging field of view could be neglected given the entrance length for the flow was very small as evidenced by the absence of transverse Dean vortices in the obtained velocity map.

4.2. Natural convection

Sample convection in liquids NMR is a known phenomenon especially with variable temperature (VT) probes in vertical bore magnets, where temperature regulated air flow from the bottom is used to maintain the sample temperature [10,34]. The nature of the fluid flows induced within the sample depend on the relative orientation between the sample temperature gradient and gravity vectors [28]. Fluid remains stationary when the temperature gradient is antiparallel to gravity, Rayleigh-Bénard (RB) convection cells are generated when the temperature gradient is parallel to gravity while Hadley cells are generated when the temperature gradient and gravity are not parallel [35]. RB convection cells begins to appear when the dimensionless Rayleigh number, Ra, reaches above a critical value, Rac, that depends on the sample geometry and wall boundary conditions [36,37]. Hadley convection cells however do not depend on any critical dimensionless number to appear and are almost always present in liquids NMR [35]. Such flows appear as a vortex which is proportional to the vector cross product of gravity and temperature gradient vectors as shown by the vorticity transport equation obtained by taking a curl of the governing Navier-Stokes equation for fluid motion [28].

To the best of our knowledge, this maybe the first report of the presence of sample convection in non-VT probes without exogenous heat sources. We posit it to occur from the differential heating of the gradient coils [38] or asymmetric sample geometry promoting heterogeneous heat transfer. Stronger axial flows (i.e. vorticity along $+\hat{x}$ using the right-hand rule) obtained in this study with gravity along $-\hat{y}$ indicate temperature gradients in $+\hat{z}$ along the bore length of the magnet based on vorticity relation described above (i.e. Hadley convection). The asymmetry in the vortex could be due to heterogeneity in the axial temperature gradient, since our magnet is enclosed at one end and has a door at the other end. The obtained velocity profile matched with experimental and computational studies of natural convection in horizontal cylinders with a small aspect ratio as in this study. Schiroky and Rosenberger reported results from laser Doppler anemometry experiments for natural convection in gases confined within a horizontal cylinder (aspect ratio = 0.1) at various Rayleigh numbers ($74 < Ra < 1.3 \times 10^6$) obtained by adjusting gas pressure and composition at a fixed axial temperature gradient [29]. They reported

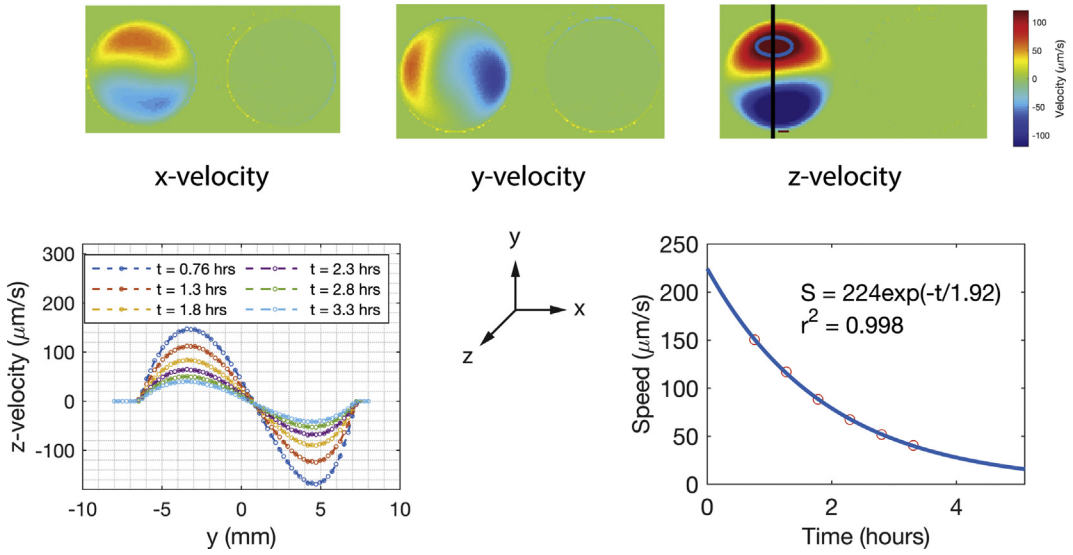

Fig. 5. PC-MRI measurement of natural convection occurring inside a horizontal cylindrical tube filled with water using stimulated echo at Ra ≈ 6000. Another tube filled with 0.6% hydrogel was placed adjacent to the water filled tube to serve as a static control. (Top row) X, Y, Z components of velocity obtained approximately 45 min after the sample was placed in the bore of the magnet. (Bottom left) Line plot of the axial (z) velocity along the black midline shown in z-velocity map for various time points, and (Bottom right) plot of the velocity magnitude averaged over the region of interest drawn in the water filled tube (both shown in z-velocity map) over time fit to an exponentially decaying function.

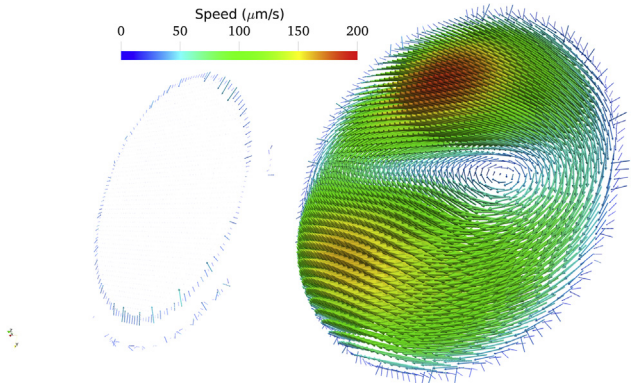

Fig. 6. 3D vector plots of natural convection inside a horizontal cylindrical tube filled with water at approximately 45 min after the sample was placed in the magnet bore. A tube filled with 0.6% hydrogel was placed on the side to serve as a static control. Vectors are colored based on the velocity magnitude.

an S-shaped axial velocity profile along the vertical mid-plane which reduced in amplitude with decreasing Rayleigh number similar to what was observed in this study with time (i.e. temperature difference between fluid and ambient reduces over time and hence the Rayleigh number reduces over time). A 3D computational fluid dynamics study by Smutek et al. solving the Navier-Stokes and energy equations with Boussinesq approximation for cylindrical geometry (aspect ratio = 0.1) and a linear axial temperature gradient also showed a similar velocity profile for 74 < Ra < 18,700 [39]. They also predicted very weak secondary azimuthal flow as observed in this study.

4.3. Feasibility for in vivo flows

Measuring creeping flows *in vivo* require unique considerations depending on the tissue of interest. In this section, a few considerations for measuring slow flows in the brain are discussed. First, background phase errors in velocity images could be introduced by the changing homogeneity of static B0 field with respiratory cycle, especially at longer echo times and/or higher B0-field strengths. DeMoortele et al. reported the homogeneity of the B0-field with humans at 7 T changes during breathing due to the changing geometry of paramagnetic air compartment in the lung which has a different magnetic susceptibility, χ_v, than the diamagnetic tissue ($\chi_v^{air} \approx +0.36$ ppm, $\chi_v^{tissue} \approx -9.06$ ppm) [40]. Secondly, it is known the brain parenchyma moves coherently throughout the cardiac cycle with peak velocities during systole up to 1.5 mm/s observed in human brain [41–43]. This motion could lead to errors in the measured velocity due to acceleration which is assumed to be zero. Thirdly, volume fraction of flowing spins in a given voxel in the brain tissue is small (blood is 10%, CSF is 10% and interstitial fluid is 12% [44]) necessitating very high spatial and velocity sensitivity to capture flows in the medium. Finally, high velocity sensitivity requires longer mixing times, which is possible given the long T1-relaxation time of brain tissue, but it also increases the minimum repetition time (TR) per slice thus prolonging the acquisition time period.

The developed flow imaging pulse sequence has very high velocity sensitivity potentially capable of resolving creeping flows present in the brain. Further improvements in flow sensitivity is possible using ultra-high-field magnets as they provide greater SNR and allow longer mixing time due to the observed increase in the brain tissue T_1 relaxation time with field strength [45]. Spatial sensitivity could be relaxed by imaging the velocity distribution within each voxel instead of the mean velocity by repeating the flow acquisition at multiple values of v_{enc} using the Fourier velocity encoding [25,46]. Effect of changing B_0-field and brain motion could be minimized by gating the pulse sequence to both cardiac and respiratory cycles such as in 4D flow MRI sequences [17]. The first TE/2 interval could be fit within one cardiac cycle with the last interval placed at the same location in a later cycle depending on the duration of the mixing time. The whole segment could then be placed in one respiratory cycle which is typically much longer than the cardiac cycle. Acquisition time could be reduced by acquiring multiple slices simultaneously (SMS) using multi-band RF excitation [47] and/or using an echo planar readout (EPI). Real-time measurement of CSF flow with cardiac and respiratory cycle has been recently reported in standard phase contrast flow MRI with SMS-EPI in humans [48].

4.4. Limitations

The accuracy of the developed method relies on properly designed gradient coils with fields that decay quickly after the gradient pulse. Presence of longer time constants might require mixing times much longer than T1 of the sample and cause greater gradient echo shifts during readout which amplify background phase errors in the flow measurement. The developed method also has an in-built slice velocity filter due to the time of flight (TOF) effect observed with spin echo imaging [49]. Flowing spins should remain within the imaged slice while the three slice-selective RF pulses are applied in order to form a stimulated echo. Thus, spins flowing with a slice velocity greater than $\frac{\Delta z}{TE+TM}$, where Δz is the slice thickness, will not generate a signal during acquisition time and hence appear with zero velocity. TOF effect has been observed previously with stimulated echoes where it was used to measure flow indirectly [50]. Finally, *in vivo* measurements spanning multiple cardiac cycles require steady heart rate and respiration otherwise a complex acquisition triggering mechanism is needed to ensure the first and last TE/2 intervals fall within the same location in the cardiac cycle. Despite these limitations, the presented method is a viable candidate for investigating creeping flows in various tissues *in vivo*.

Grant support

This work is supported in part by the NIH/NCATS Clinical and Translational Science Award UL1 TR000064, and National High Magnetic Field Laboratory pilot study grant awarded to Dr. Lonser.

Acknowledgments

A portion of this work was performed in the Advanced MRI/S (AMRIS) Facility at the McKnight Brain Institute of the University of Florida, which is part of the National High Magnetic Field Laboratory (NHMFL) supported by National Science Foundation Cooperative Agreement DMR-1157490, the State of Florida, and the U.S. Department of Energy. We would like to thank Dr. Alan Rath from Agilent Technologies for advice on pulse programming, and Dr. Huadong Zeng and Kelly Jenkins from the AMRIS facility for assisting with experimental setup. We would also like to thank Julian Rey for helping with the pipe flow experimental setup.

Appendix A. Simplification of flow induced phase change due to bipolar gradient

A typical 1D bipolar flow encoding gradient, $G_{flow}(t)$, is given by,

$$G_{flow}(t) = \begin{cases} g(t) & 0 \leqslant t \leqslant \delta \\ 0 & \delta \leqslant t \leqslant \Delta \\ -g(t-\Delta) & \Delta \leqslant t \leqslant \Delta + \delta \end{cases} \tag{A1}$$

The phase, ϕ, induced by spins steadily flowing with velocity, v, along the direction of this flow-encoding gradient is given by,

$$\phi = -\gamma v \int_0^{\Delta+\delta} t G_{flow}(t) dt \tag{A2}$$

$$= -\gamma v \left[\underbrace{\int_0^{\delta} t g(t) dt}_{I_1} - \underbrace{\int_{\Delta}^{\Delta+\delta} t g(t-\Delta) dt}_{I_2} \right] \tag{A3}$$

Changing variable in I_2 with $t' = t - \Delta$ results in

$$I_2 = \int_0^{\delta} (t' + \Delta) g(t') dt' \tag{A4}$$

$$= \int_0^{\delta} t' g(t') dt' + \Delta \int_0^{\delta} g(t') dt' \tag{A5}$$

Substituting Eq. (A5) into Eq. (A3),

$$\phi = -\gamma v [I_1 - I_2] = vq\Delta \tag{A6}$$

where,

$$q = \gamma \int_0^{\delta} g(t) dt \tag{A7}$$

References

[1] A.F. Frydrychowski, A. Szarmach, B. Czaplewski, P.J. Winklewski, Subarachnoid space: new tricks by an old dog, PLoS One 7 (2012) e37529, https://doi.org/10.1371/journal.pone.0037529.
[2] J.H. Kim, T.H. Mareci, M. Sarntinoranont, A voxelized model of direct infusion into the corpus callosum and hippocampus of the rat brain: model development and parameter analysis, Med. Biol. Eng. Comput. 48 (2010) 203–214, https://doi.org/10.1007/s11517-009-0564-7.
[3] K.N. Magdoom, G.L. Pishko, L. Rice, C. Pampo, D.W. Siemann, M. Sarntinoranont, MRI-based computational model of heterogeneous tracer transport following local infusion into a mouse hind limb tumor, PLoS One 9 (2014), https://doi.org/10.1371/journal.pone.0089594.
[4] J.M. Munson, A.C. Shieh, Interstitial fluid flow in cancer: implications for disease progression and treatment, Cancer Manage. Res. 6 (2014) 317, https://doi.org/10.2147/CMAR.S65444.
[5] M. Asgari, D. de Zélicourt, V. Kurtcuoglu, Glymphatic solute transport does not require bulk flow, Sci. Rep. 6 (2016) 38635, https://doi.org/10.1038/srep38635.
[6] C. Blatter, E.F.J. Meijer, A.S. Nam, D. Jones, B.E. Bouma, T.P. Padera, B.J. Vakoc, In vivo label-free measurement of lymph flow velocity and volumetric flow rates using Doppler optical coherence tomography, Sci. Rep. 6 (2016) 29035, https://doi.org/10.1038/srep29035.
[7] S.R. Chary, R.K. Jain, Direct measurement of interstitial convection and diffusion of albumin in normal and neoplastic tissues by fluorescence photobleaching, Proc. Natl. Acad. Sci. U. S. A. 86 (1989) 5385–5389, https://doi.org/10.1073/PNAS.86.14.5385.
[8] T. Hompland, C. Ellingsen, K.M. Ovrebo, E.K. Rofstad, Interstitial fluid pressure and associated lymph node metastasis revealed in tumors by dynamic contrast-enhanced MRI, Cancer Res. 72 (2012) 4899–4908, https://doi.org/10.1158/0008-5472.CAN-12-0903.
[9] R. Elmghirbi, T.N. Nagaraja, S.L. Brown, K.A. Keenan, S. Panda, G. Cabral, H. Bagher-Ebadian, G.W. Divine, I.Y. Lee, J.R. Ewing, Toward a noninvasive estimate of interstitial fluid pressure by dynamic contrast-enhanced MRI in a rat model of cerebral tumor, Magn. Reson. Med. (2018), https://doi.org/10.1002/mrm.27163.
[10] P.T. Callaghan, Translational Dynamics and Magnetic Resonance: Principles of Pulsed Gradient Spin Echo NMR, Oxford University Press, 2011.
[11] H. Wassenius, P.T. Callaghan, Nanoscale NMR velocimetry by means of slowly diffusing tracer particles, J. Magn. Reson. 169 (2004) 250–256, https://doi.org/10.1016/j.jmr.2004.05.005.
[12] D. Benjamini, M.E. Komlosh, N.H. Williamson, P.J. Basser, Generalized mean apparent propagator (GMAP) MRI to measure and image advective and dispersive flows in medicine and biology 1–1 IEEE Trans. Med. Imag. (2018), https://doi.org/10.1109/TMI.2018.2852259.
[13] T.W.J. Scheenen, F.J. Vergeldt, C.W. Windt, P.A. De Jager, H. Van As, Microscopic imaging of slow flow and diffusion: a pulsed field gradient stimulated echo sequence combined with turbo spin echo imaging, J. Magn. Reson. 151 (2001) 94–100, doi:10.1006.
[14] L.A. Rivera-Rivera, P. Turski, K.M. Johnson, C. Hoffman, S.E. Berman, P. Kilgas, H. A. Rowley, C.M. Carlsson, S.C. Johnson, O. Wieben, 4D flow MRI for intracranial hemodynamics assessment in Alzheimer's disease, J. Cereb. Blood Flow Metab. 36 (2016) 1718–1730, https://doi.org/10.1177/0271678X15617171.
[15] M.J. McGirt, S.M. Nimjee, H.E. Fuchs, T.M. George, Relationship of cine phase-contrast magnetic resonance imaging with outcome after decompression for Chiari I malformations, Neurosurgery 59 (2006), https://doi.org/10.1227/01.NEU.0000219841.73999.B3, discussion 140-6.
[16] M. Mase, K. Yamada, T. Banno, T. Miyachi, S. Ohara, T. Matsumoto, Quantitative analysis of CSF flow dynamics using MRI in normal pressure hydrocephalus, in: Intracranial Press. Neuromonitoring Brain Inj., Springer Vienna, Vienna, 1998, pp. 350–353, https://doi.org/10.1007/978-3-7091-6475-4_101.
[17] M. Markl, A. Frydrychowicz, S. Kozerke, M. Hope, O. Wieben, 4D flow MRI, J. Magn. Reson. Imag. 36 (2012) 1015–1036, https://doi.org/10.1002/jmri.23632.
[18] D. Giese, M. Haeberlin, C. Barmet, K.P. Pruessmann, T. Schaeffter, S. Kozerke, Analysis and correction of background velocity offsets in phase-contrast flow measurements using magnetic field monitoring, Magn. Reson. Med. 67 (2012) 1294–1302, https://doi.org/10.1002/mrm.23111.

[19] J. Busch, S.J. Vannesjo, C. Barmet, K.P. Pruessmann, S. Kozerke, Analysis of temperature dependence of background phase errors in phase-contrast cardiovascular magnetic resonance, J. Cardiovasc. Magn. Reson. 16 (2014) 97, https://doi.org/10.1186/s12968-014-0097-6.
[20] M.A. Bernstein, X.J. Zhou, J.A. Polzin, K.F. King, A. Ganin, N.J. Pelc, G.H. Glover, Concomitant gradient terms in phase contrast MR: analysis and correction, Magn. Reson. Med. 39 (1998) 300–308.
[21] P.G. Walker, G.B. Cranney, M.B. Scheidegger, G. Waseleski, G.M. Pohost, A.P. Yoganathan, Semiautomated method for noise reduction and background phase error correction in MR phase velocity data, J. Magn. Reson. Imag. 3 (1993) 521–530, https://doi.org/10.1002/jmri.1880030315.
[22] L. Huang, G. Mikolajczyk, E. Küstermann, M. Wilhelm, S. Odenbach, W. Dreher, Adapted MR velocimetry of slow liquid flow in porous media, J. Magn. Reson. 276 (2017) 103–112, https://doi.org/10.1016/J.JMR.2017.01.017.
[23] S. Walker-Samuel, T.A. Roberts, R. Ramasawmy, J.S. Burrell, S.P. Johnson, B.M. Siow, S. Richardson, M.R. Gonçalves, D. Pendse, S.P. Robinson, R.B. Pedley, M.F. Lythgoe, Investigating low-velocity fluid flow in tumors with convection-MRI, Cancer Res. 78 (2018) 1859–1872, https://doi.org/10.1158/0008-5472.CAN-17-1546.
[24] M. Soellinger, A.K. Rutz, S. Kozerke, P. Boesiger, 3D cine displacement-encoded MRI of pulsatile brain motion, Magn. Reson. Med. 61 (2009) 153–162, https://doi.org/10.1002/mrm.21802.
[25] E.M. Haacke, R.W. Brown, M.R. Thompson, R. Venkatesan, Magnetic Resonance Imaging: Physical Principles and Sequence Design, Wiley, 1999 (accessed November 8, 2013) http://books.google.com/books/about/Magnetic_Resonance_Imaging.html?id=BnOvQgAACAAJ&pgis=1.
[26] N.J. Pelc, M.A. Bernstein, A. Shimakawa, G.H. Glover, Encoding strategies for three-direction phase-contrast MR imaging of flow, J. Magn. Reson. Imag. 1 (1991) 405–413 (accessed October 8, 2013) http://onlinelibrary.wiley.com/doi/10.1002/jmri.1880010404/full.
[27] P.S. Tofts, D. Lloyd, C.A. Clark, G.J. Barker, G.J. Parker, P. McConville, C. Baldock, J.M. Pope, Test liquids for quantitative MRI measurements of self-diffusion coefficient in vivo, Magn. Reson. Med. 43 (2000) 368–374. http://www.ncbi.nlm.nih.gov/pubmed/10725879.
[28] D.J. Tritton, Physical Fluid Dynamics, Clarendon Press, 1988 (accessed September 20, 2018) https://global.oup.com/ushe/product/physical-fluid-dynamics-9780198544937?cc=us&lang=en&.
[29] G.H. Schiroky, F. Rosenberger, Free convection of gases in a horizontal cylinder with differentially heated end walls, Int. J. Heat Mass Transf. 27 (1984) 587–598, https://doi.org/10.1016/0017-9310(84)90031-0.
[30] M.A. Schofield, Y. Zhu, Fast phase unwrapping algorithm for interferometric applications, Opt. Lett. 28 (2003) 1194–1196, https://doi.org/10.1364/OL.28.001194.
[31] C.D. Hansen, C.R. Johnson, The Visualization Handbook, Elsevier Butterworth-Heinemann, 2005 (accessed September 20, 2018) https://www.sciencedirect.com/book/9780123875822/visualization-handbook.
[32] Z. Püspöki, M. Storath, D. Sage, M. Unser, Transforms and operators for directional bioimage analysis: a survey, in: Adv. Anat. Embryol. Cell Biol., 2016, pp. 69–93, https://doi.org/10.1007/978-3-319-28549-8_3.
[33] J. Schindelin, I. Arganda-Carreras, E. Frise, V. Kaynig, M. Longair, T. Pietzsch, S. Preibisch, C. Rueden, S. Saalfeld, B. Schmid, J.-Y. Tinevez, D.J. White, V. Hartenstein, K. Eliceiri, P. Tomancak, A. Cardona, Fiji: an open-source platform for biological-image analysis, Nat. Methods 9 (2012) 676–682, https://doi.org/10.1038/nmeth.2019.
[34] I. Swan, M. Reid, P.W.A. Howe, M.A. Connell, M. Nilsson, M.A. Moore, G.A. Morris, Sample convection in liquid-state NMR: why it is always with us, and what we can do about it, J. Magn. Reson. 252 (2015) 120–129, https://doi.org/10.1016/j.jmr.2014.12.006.
[35] M. Lappa, Thermal Convection: Patterns, Evolution and Stability, Wiley, 2010 (accessed September 20, 2018) https://books.google.com/books?hl=en&lr=&id=Cvn1czoCYxgC&oi=fnd&pg=PR7&dq=Thermal+convection:+patterns,+evolution+and+stability&ots=b7qoOUzUHU&sig=Xxn6j1e9oEt742JehyW6MKQGZmc#v=onepage&q=Thermal convection%3A patterns%2C evolution and stability&f=false.
[36] G. Charlson, R. Sani, Thermoconvective instability in a bounded cylindrical fluid layer, Int. J. Heat Mass Transf. 13 (1970) 1479–1496, https://doi.org/10.1016/0017-9310(70)90181-X.
[37] P.G. Drazin, W.H. Reid, Hydrodynamic Stability, Cambridge University Press, 2004.
[38] P.T. While, L.K. Forbes, S. Crozier, Calculating temperature distributions for gradient coils, Concepts Magn. Reson. Part B Magn. Reson. Eng. 37B (2010) 146–159, https://doi.org/10.1002/cmr.b.20163.
[39] C. Smutek, P. Bontoux, B. Roux, G.H. Schiroky, A.C. Hurford, F. Rosenberger, G. de Vahl Davis, Three-dimensional convection in horizontal cylinders: numerical solutions and comparison with experimental and analytical results, Numer. Heat Transf. 8 (1985) 613–631, https://doi.org/10.1080/01495728508961875.
[40] P.-F. Van de Moortele, J. Pfeuffer, G.H. Glover, K. Ugurbil, X. Hu, Respiration-induced B0 fluctuations and their spatial distribution in the human brain at 7 Tesla, Magn. Reson. Med. 47 (2002) 888–895, https://doi.org/10.1002/mrm.10145.
[41] D. Greitz, R. Wirestam, A. Franck, B. Nordell, C. Thomsen, F. Ståhlberg, Pulsatile brain movement and associated hydrodynamics studied by magnetic resonance phase imaging. The Monro-Kellie doctrine revisited, Neuroradiology 34 (1992) 370–380, https://doi.org/10.1007/BF00596493.
[42] B.P. Poncelet, V.J. Wedeen, R.M. Weisskoff, M.S. Cohen, Brain parenchyma motion: measurement with cine echo-planar MR imaging, Radiology 185 (1992) 645–651, https://doi.org/10.1148/radiology.185.3.1438740.
[43] M.E. Wagshul, P.K. Eide, J.R. Madsen, The pulsating brain: A review of experimental and clinical studies of intracranial pulsatility, Fluids Barriers CNS 8 (2011) 5, https://doi.org/10.1186/2045-8118-8-5.
[44] A.S. Thrane, V. Rangroo Thrane, M. Nedergaard, Drowning stars: reassessing the role of astrocytes in brain edema, Trends Neurosci. 37 (2014) 620–628, https://doi.org/10.1016/J.TINS.2014.08.010.
[45] W.D. Rooney, G. Johnson, X. Li, E.R. Cohen, S.-G. Kim, K. Ugurbil, C.S. Springer, Magnetic field and tissue dependencies of human brain longitudinal $1H_2O$ relaxation in vivo, Magn. Reson. Med. 57 (2007) 308–318, https://doi.org/10.1002/mrm.21122.
[46] C.K. Macgowan, C.J. Kellenberger, J.S. Detsky, K. Roman, S.-J. Yoo, Real-time fourier velocity encoding: an in vivo evaluation, J. Magn. Reson. Imag. 21 (2005) 297–304, https://doi.org/10.1002/jmri.20266.
[47] D.J. Larkman, J.V. Hajnal, A.H. Herlihy, G.A. Coutts, I.R. Young, G. Ehnholm, G. Sta Ehnholm, Use of multicoil arrays for separation of signal from multiple slices simultaneously excited, J. Magn. Reson. Imag. 13 (2001) 313–317, https://doi.org/10.1002/1522-2586(200102)13:2<313::AID-JMRI1045>3.0.CO;2-W.
[48] L. Chen, A. Beckett, A. Verma, D.A. Feinberg, Dynamics of respiratory and cardiac CSF motion revealed with real-time simultaneous multi-slice EPI velocity phase contrast imaging, Neuroimage 122 (2015) 281–287, https://doi.org/10.1016/j.neuroimage.2015.07.073.
[49] D.W. McRobbie, E.A. Moore, M.J. Graves, M.R. Prince, MRI from Picture to Proton, Cambridge University Press, 2003.
[50] K.-D. Derboldt, W. Hänicke, J. Frahm, Flow NMR imaging using stimulated echoes, J. Magn. Reson. 67 (1986) 336–341, https://doi.org/10.1016/0022-2364(86)90438-5.